# Fluorescent Drug-Loaded, Polymeric-Based, Branched Gold Nanoshells for Localized Multimodal Therapy and Imaging of Tumoral Cells

**Antonio Topete,[†] Manuel Alatorre-Meda,[†,§,⊥] Pablo Iglesias,[‡] Eva M. Villar-Alvarez,[†] Silvia Barbosa,[†,*] José A. Costoya,[‡] Pablo Taboada,[†,*] and Víctor Mosquera[†]**

[†]Grupo de Física de Coloides y Polímeros, Departamento de Física de la Materia Condensada, Universidad de Santiago de Compostela, Santiago de Compostela 15782, Spain and [‡]Grupo de Oncología Molecular, Centro de Investigación en Medicina Molecular y Enfermedades Crónicas (CIMUS), Universidad de Santiago de Compostela, Santiago de Compostela 15782, Spain. [§]Present address: 3B's Research Group-Biomaterials, Biodegradables and Biomimetics, University of Minho, Headquarters of the European Institute of Excellence on Tissue Engineering and Regenerative Medicine, AvePark, Zona Idustrial da Gandra, S. Claudio do Barco, Caldas das Taipas, Guimarães, 48-909, Portugal. [⊥]Present address: ICVS/3B's-PT Government Associate Laboratory, Braga, Guimarães, Portugal.

**ABSTRACT** Here we report the synthesis of PLGA/DOXO-core Au-branched shell nanostructures (BGNSHs) functionalized with a human serum albumin/indocyanine green/folic acid complex (HSA-ICG-FA) to configure a multifunctional nanotheranostic platform. First, branched gold nanoshells (BGNSHs) were obtained through a seeded-growth surfactant-less method. These BGNSHs were loaded during the synthetic process with the chemotherapeutic drug doxorubicin, a DNA intercalating agent and topoisomerase II inhibitior. In parallel, the fluorescent near-infrared (NIR) dye indocyanine green (ICG) was conjugated to the protein human serum albumin (HSA) by electrostatic and hydrophobic interactions. Subsequently, folic acid was covalently attached to the HSA-ICG complex. In this way, we created a protein complex with targeting specificity and fluorescent imaging capability. The resulting HSA-ICG-FA complex was adsorbed to the gold nanostructures surface (BGNSH-HSA-ICG-FA) in a straightforward incubation process thanks to the high affinity of HSA to gold surface. In this manner, BGNSH-HSA-ICG-FA platforms were featured with multifunctional abilities: the possibility of fluorescence imaging for diagnosis and therapy monitoring by exploiting the inherent fluorescence of the dye, and a multimodal therapy approach consisting of the simultaneous combination of chemotherapy, provided by the loaded drug, and the potential cytotoxic effect of photodynamic and photothermal therapies provided by the dye and the gold nanolayer of the hybrid structure, respectively, upon NIR light irradiation of suitable wavelength. The combination of this trimodal approach was observed to exert a synergistic effect on the cytotoxicity of tumoral cells *in vitro*. Furthermore, FA was proved to enhance the internalization of nanoplatform. The ability of the nanoplatforms as fluorescence imaging contrast agents was tested by preliminary analyzing their biodistribution *in vivo* in a tumor-bearing mice model.

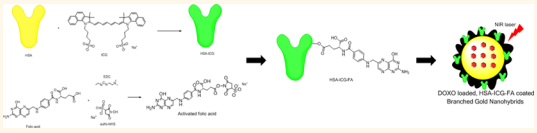

**KEYWORDS:** nanotheranosis · photodynamic therapy · photothermal therapy · light-triggered drug release · *in vivo* fluorescence imaging

One of the areas of nanotechnology that has captured great interest by scientific community worldwide is the development of nanoengineered multifunctional systems, which may be potentially used in a clinical strategy that simultaneously combine a (multi)diagnostic test and single or combined therapies based on the test results, the so-called nanotheranostic devices.[1−7] Nanoengineering of materials for this purpose involves the design, fabrication, and testing of nanosystems that must combine several features such as biocompatibility, stealthness, long-circulating blood times, drug transport and its triggerable release, imaging capabilities, and/or targetability, among others.[8−12] Improvement and suitable conjunction of all these characteristics would allow the early diagnosis of cancer and other diseases, the significant reduction of the therapeutic drug doses and subsequent reduction of adverse side effects, or the simultaneous combination of several therapeutic treatments with a real-time monitorization of their effectiveness.[1,3,9,10]

Among all the different diagnostic imaging techniques, fluorescence imaging offers

* Address correspondence to silvia.barbosa@usc.es, pablo.taboada@usc.es.

Received for review December 16, 2013 and accepted February 26, 2014.

**Published online February 26, 2014**
**10.1021/nn406425h**

a unique approach for visualizing morphological details in tissue with subcellular resolution, and becomes a powerful noninvasive tool for visualizing the full range of biospecies from living cells to animals. Most of the conventional fluorescence probes for bioimaging are based on single-photon excitation, emitting low energy fluorescence when excited by high energy light. These probes have some limitations: (i) DNA damage and cell death due to long-term exposure to high energy excitation, (ii) low signal-to-noise ratio caused by significant autofluorescence from the biological tissues, (iii) and low penetration depth in the biological tissues. Compared with visible light excitation, near-infrared (NIR) light excitation of NIR contrast agents for *in vivo* imaging provides several advantages such as deep penetration, weak autofluorescence, reduced photobleaching, and low phototoxicity.[13,14] In addition, these NIR probes can be simultaneously used under exposition to NIR light as phototherapeutic agents, acting as efficient photosensitizers transforming endogeneous oxygen to singlet oxygen ($^1O_2$) to kill cancer cells, the so-called photodynamic therapy (PDT).[15−17] Because this therapy is based on direct light administration to tumors/tissues, PDT treatment has remarkably improved tumor selectivity and reported side effects as compared to conventional chemo- and radiotherapies.[18,19] However, PDT efficacy in tumors is largely limited by different factors such as the inadequate selectivity and poor water solubility of most photosensitizers,[18,20−24] the self-destruction of photosensitizers upon light irradiation,[25,26] the depletion of tissue oxygen, and the disruption of tumor blood flow, which causes severe local hypoxia and cease the production of $^1O_2$,[27,28] hindering the therapeutic efficacy of PDT and restricting its potential application in clinics.[29]

On the other hand, novel plasmonic photothermal effects of gold nanostructures such as gold nanorods and nanostars,[30−34] nanoshells,[35−37] carbon nanotubes[38−41] or graphene oxide[42−44] activated by NIR light illumination are being actively studied for their tumoricidal efficacies. Nevertheless, while these nanomaterials can certainly increase the local temperature around cancerous regions upon exposition to NIR light, it is not entirely evident that the photothermal effect is sufficient to achieve the desired level of cancer-cell cytotoxicity with a wide range.[45,46] Thus, for patient compliance, the development of nanosystems for largely enhancing the tumoricidal efficacy by combination of different therapeutic approaches is vital and can allow to overcome current limitations of single available therapies and lead to synergistic cytotoxic effects.[47−49]

Hence, with the aim to simultaneously combine chemo-, photo-, and thermotherapies with fluorescence imaging capability for diagnosis under NIR light illumination, we here developed a multifunctional nanoplatform consisting of a poly(lactic-*co*-glycolic acid) (PLGA) biodegradable matrix loaded with the anticancer drug doxorubicin (DOXO). The polymeric PLGA nanoparticle (NP) was covered with a porous gold shell, which provides the nanoplatform the ability of NIR light absorption and subsequent efficient energy transduction in the form of localized heat due to NIR resonance of the metal shell, and also accelerates drug release from the nanoplatform.[50] The nanoshell surface was functionalized with the plasma protein human serum albumin (HSA) for stealthiness to which the fluorescent dye indocyanine green (ICG) was noncovalently conjugated to provide the nanoplatform with fluorescence imaging and singlet oxygen production capabilities. ICG is a tricarbocyanine dye with absorbing properties exclusively in the NIR electromagnetic spectrum, and currently used as a diagnostic agent for blood volume determination, ophtalmic angiography, cardiac output, and hepatic function.[51,52] In addition, folic acid was also covalently conjugated to the protein surface to provide the nanoplatform with specific targetability. In this way, heat, singlet oxygen species, and drug could be simultaneously delivered to the selected tumor region. We demonstrated that the present nanoplatforms showed synergistic therapeutic effects *in vitro* by combination of chemo-, photo-, and thermotherapies, and can simultaneously act as effective contrast agents for *in vivo* optical imaging by exploiting the fluorescence enhancement of the dye upon positioning near the metal surface while tuning the plasmon resonance of the nanoshell to the emission wavelength of the fluorophore.[53]

## RESULTS AND DISCUSSION

The fabrication procedure of the hybrid nanoplatforms is represented in Supporting Information Figure S1. DOXO-loaded PLGA NPs stabilized with low molecular weight chitosan biopolymer were prepared by a modified nanoprecipitation method (see Methods section for details). The drug loading capacity, defined as the amount of drug loaded inside the loaded polymeric matrix, was estimated to be 3.9% (w/w). Next, citrated stabilized Au seeds (4 nm) were deposited onto the surface of chitosan-modified DOXO-loaded PLGA NPs, and a full and porous metal shell structure was obtained in the presence of a growth solution exclusively composed of $HAuCl_4$, $K_2CO_3$, and ascorbic acid (AA).[54] Trasmission and scanning electron microscopies confirmed the morphology of the hybrid gold nanoshells (BGNSHs), which resemble a virus capside (Figure 1a,b) with a size of *ca.* 85 ± 15 nm. The ultraviolet−visible/NIR absorption spectrum of BGNSHs exhibited a pronounced surface plasmon absorption in the NIR region ($\lambda \approx 770$ nm, Figure 1c) consistent with a reticular Au shell formed around the dielectric polymeric core of the nanoplatform. In the absence of the metal shell, the DOXO-loaded PLGA NPs

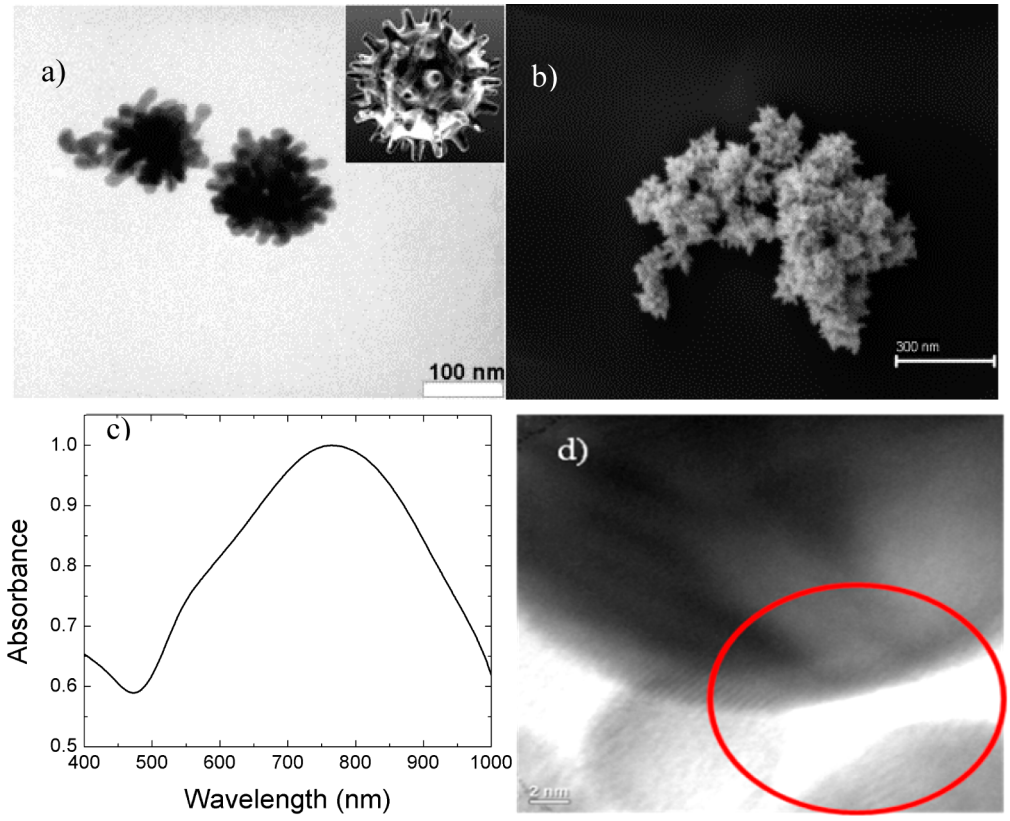


**Figure 1. (a) TEM image of BGNSHs nanoplatforms. The inset shows a virus particle confirming the biomimetic shape of the synthesized nanoplatforms. (b) SEM image of BGNSHS. (c) UV−vis absorption spectrum of BGNSHs. (d) HRTEM image of BGNSHs showing the existence of voids in the Au shell structure.**

exhibited absorption maxima at $\lambda \approx 490$ nm, in agreement with the absorbance peak of free DOXO. Electron diffraction X-ray spectroscopy (EDX) showed traces of C and O elements from the polymeric inner components and Au corresponding to the metal shell, which was a first evidence of the porous nature of the metal shell (Supporting Information Figure S2). This was additionally confirmed while examining high-resolution TEM (HR-TEM) images, where the existence of voids or pores on the metal layer could be observed (Figure 1d).

The Au surface of the hybrid BGNSHs was functionalized with HSA-ICG or HSA-ICG-FA (when corresponding) complexes to improve the stability and impart full stealthiness to these nanoplatforms under physiological conditions.[55−57] HSA possess a great affinity for gold surfaces and it tends to spontaneously adsorb onto them. This strong adsorption can originate from the combination of electrostatic, van der Waals and thiol-Au bonding, the latter provided by the thiol groups of the protein's cysteine residues. Besides the stabilizing effect, the protein layer can also act as a biocompatible cover which reduces the nonspecific adsorption of opsonines and macrophage recognition.[58,59] To configure the HSA-ICG-FA complexes, ICG was noncovalently attached to the protein. Subsequently, FA was covalently conjugated by carbodiimide chemistry to the amine groups of the surface lysine

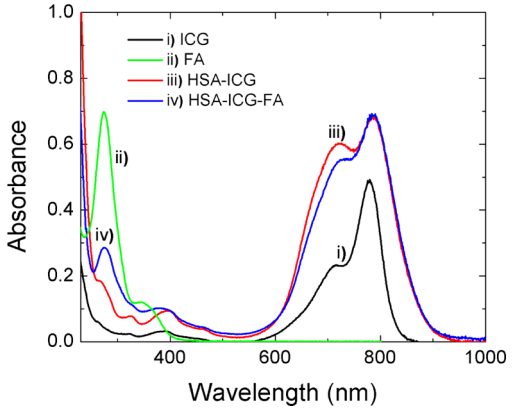


**Figure 2. UV−vis spectra of free ICG, free FA, and HSA-ICG and HSA-ICG-FA complexes after 24 h of dialysis showing the ICG and FA characteristic peaks.**

residues of the protein molecules (Supporting Information Figure S3). The successful anchoring of ICG to HSA was easily evidenced by the presence of absorbance peaks at *ca.* 780 nm corresponding to the protein complex (in the absence of BGNSHs), and arising from the dye fluorescence, and at 278 and 385 nm (Figure 2) corresponding to FA UV−vis absorption. Changes in $\zeta$-potential of the protein from $-5.6 \pm 2.3$ to $-27.6 \pm 4.6$ mV were observed at different stages of the conjugation process (Supporting Information Table S1).

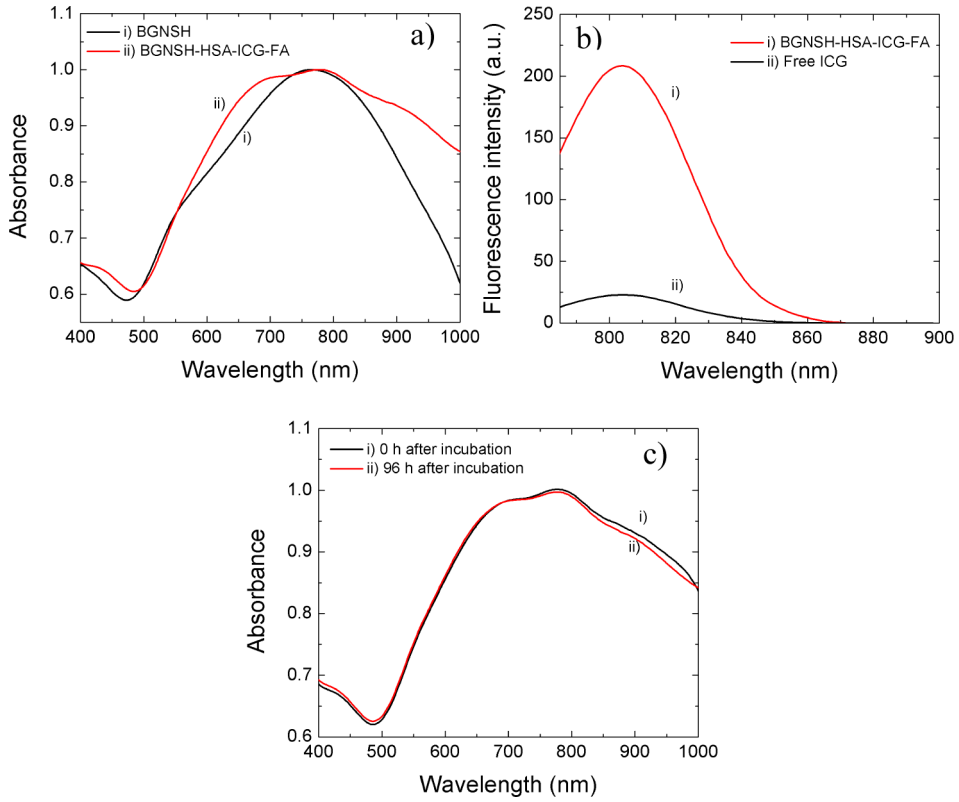


**Figure 3. (a) UV−vis spectra of bare (i) BGNSHS and (ii) BGNSH-HSA-ICG-FA in PBS with 10% (v/v) FBS. (b) Fluorescence spectra of (i) BGNSH-HSA-ICG-FA (with 5 $\mu$M of conjugated ICG) and free (ii) ICG (5 $\mu$M). (c) UV−vis spectra of BGNSH-HSA-ICG-FA in PBS with 10% (v/v) FBS (i) right after incubation and (ii) after 96 h of storage at room temperature.**

Incubation of the protein complexes in the presence of the hybrid gold nanoshells led to the formation of BGNSH-HSA-ICG-FA nanoplatforms. The successful conjugation of the HSA-ICG-FA complex to BGNSHs was confirmed, on one hand, by a slight red-shift and broadening of the LSPR band of the metal nanoshell due to the higher refractive index of HSA[60,61] and the light absorbance of bounded ICG (Figure 3a) and, on the other, by the increase and blue-shift of the ICG fluorescence peak upon protein complex adsorption onto the nanoplatform surface (Figure 3b). The sizes of BGNSH-HSA-ICG-FA nanoplatforms were determined by dynamic light scattering (DLS) approximately to be $\sim 135 \pm 25$ nm, with an effective $\zeta$-potential of $-16.3 \pm 1.7$ mV (Supporting Information Table S2). The 30 nm increase in size if compared with bare BGNSHs is consistent with the formation of a protein multilayer onto the gold surfaces, in agreement with previous reports.[62] We then determined the gold concentration of BGNHS-HSA-ICG-FA (or BGNHS-HSA-ICG) by inductively coupled plasma−mass spectroscopy (ICP-MS). Combination of ICP-MS (to determine the nanoshell concentration in solution) and UV−vis spectroscopy data (to determine the ICG complexed concentration) showed that *ca.* 450 ICG molecules were anchored per BGNSHS nanoplatform.

BGNSH-HSA-ICG-FA nanoplatforms exhibited excellent dispersivity and stability in, for example, PBS containing 10% (v/v) FBS (Figure 3c and Supporting Information Figure S4), with no aggregates observed by the naked eye or optical microscopy.

To know whether the nanoplatform structure enables a simultaneous effective DOXO release through the porous Au layer and photodynamic- and photothermal-induced tumoricidal effects using NIR light (because of minimal absorption by water and hemoglobin at this wavelength range), we explored the photophysical and photochemical properties of BGNSH-HSA-ICG-FA nanoplatforms. As a first step, we compared the fluorescence intensity of BGNSH-HSA-ICG-FA particles and free ICG molecules. We observed that the fluorescence of ICG was enhanced once adsorbed onto the metal shell surface (as a part of the protein complex) due to a metal enhanced fluorescence effect (Figure 3b). It has been previously shown that ICG fluorescence enhancement takes place upon dye adsorption onto a metal surface at separation distances between 7 and 50 nm.[53] This enhacement suggested the formation of a multilayer protein structure on the BGNSHs nanoplatforms, which efficiently separated the dye molecules from the metal surface avoiding their fluorescence quenching by the strong BGNSHs surface plasmonic effect.

To evaluate the potential hyperthermic potential of the nanoplatforms, temperature increases generated by NIR laser irradiation (808 nm and 2 W cm$^{-2}$ for

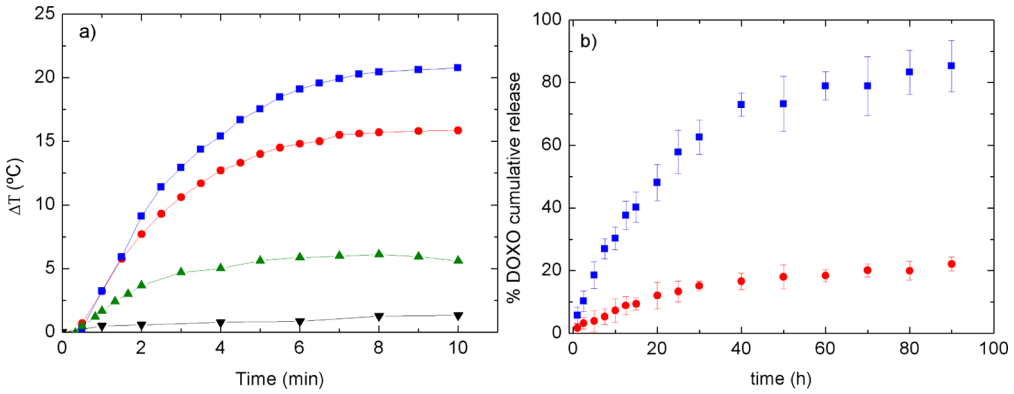


**Figure 4. (a) Temperature increases as a function of time under NIR light irradiation (808 nm at 2 W cm$^{-2}$) of (▼) PBS buffer solution with 10% (v/v) FBS, (●) BGNSHs, (▲) free ICG, and (■) BGNSH-HSA-ICG-FA. (b) Release profile of DOXO from DOXO-loaded BGNSH-HSA-ICG-FA nanoplatforms in the (●) absence and (■) presence of NIR irradiation (10 min).**

10 min) of the present hybrid nanoplatforms were measured (Figure 4a). The temperature of BGNSH-HSA-ICG-FA solutions increased by *ca.* 19 °C after 5 min of irradiation, compared to *ca.* 15, 6, and 1 °C of BGNSH-HSA particles, free ICG molecules, and buffer solutions, respectively. We also noted that the temperature rose rapidly within 3−4 min of irradiation, lying in a quasiplateau region afterward. These results demonstrated the latent capability of the present nanoplatforms for hyperthermia or ablation of cancer cells, which can be additionally enhanced thanks to the suitable selection of the shell material and thickness (the HSA layer doped with ICG) with strong absorption in the NIR region.[63] Moreover, the heat generated by the nanoplatforms under NIR irradiation was sufficient to overcome the glass transition temperature of PLGA (*ca.* 45 °C) to induce a sudden drug release of DOXO from nanoplatforms followed by a slower diffusion release phase. The amount of drug released was steeply increased (Figure 4b), coincident with NIR laser irradiation, which is certainly useful for increasing the tumoricidal effect of the present nanoplatforms.

The possibility of using the BGNSH-HSA-ICG-FA nanoplatforms as potential PDT agents was tested by measuring their $^1O_2$ generation capability under laser irradiation at 808 nm. Given that photodegradation may greatly restrict the efficiency of the nanoplatforms as potential PDT and PPT agents, we investigated the photostability of free ICG, BGNSH-HSA and BGNSH-HSA-ICG-FA nanoparticles. First, the stability of the fluorescence signal corresponding to ICG complexed to the nanoplatform was greatly enhanced if compared with that of free ICG at a similar concentration (5 $\mu$M): While free ICG fluorescence intensity decreases up to 50% in two days and 7% in one week, complexed ICG maintained ∼55% of its original fluorescence after almost one month under storage (Figure 5a). As commented previously, ICG complexation with HSA protein involves an enhancement of dye's steric stabilization which reduces the mobility of the fluorophore in aqueous solution, hence resulting in a higher dye stability and a decreased in fluorescence lifetime and increase in quantum yield.[37,64] NIR irradiation of the nanoplatforms for different time periods showed that the fluorescence of ICG at *ca.* 810 nm decreased immediately after NIR illumination and almost disappeared after 15 min at 4 and 6 W cm$^{-2}$ power density, while it barely changed after 30 min of persistent irradiation at 2 W cm$^{-2}$ (Figure 5b). It is worth noting that both LSPR of BGNSHs at 770 nm and nanoplatform morphology did not change under the latter irradiation conditions (Figure 5c). These facts evidenced that BGNSHs were very stable upon continuous wave (CW) laser irradiation at the selected NIR irradiation power and duration, while complexed ICG molecules undergo certain photobleaching regardless anchored on BGNSHs. At larger irradiation powers, a melting of the spikes (Figure 5d) leads to a progressive smoothness of the particle surfaces due to the high localized temperature increment on their surroundings, which can even give rise to a complete breakage of the nanoplatforms (Supporting Information Figure S5). Therefore, on the basis of both photothermal and fluorescence stability responses, it seems that an irradiation power of 2 W cm$^{-2}$ might be potentially suitable to achieve a combinatorial approach to enhance enhance cytotoxicity through the stimulated and controlled drug release under irradiation, the photothermal effect of the nanoplatforms and their potential photodynamic activity while avoiding drawbacks associated with larger irradiation intensities and/or exposure times such as nanoplatform instability.

The generation of $^1O_2$ was quantitatively determined by following the absorbance intensity decay of 1,3-diphenylisobenzofurane (DPIBF) at 420 nm, which is a specific singlet oxygen trap.[65] On the basis of the photostability results, we tested the $^1O_2$ production after a maximum time of 30 min of illumination. $^1O_2$ production was observed to increase (DPIBF absorbance decrease) until 20 min of continuous laser irradiation and then, it reaches a quasi plateau region, which certainly indicates that an effective reduction in

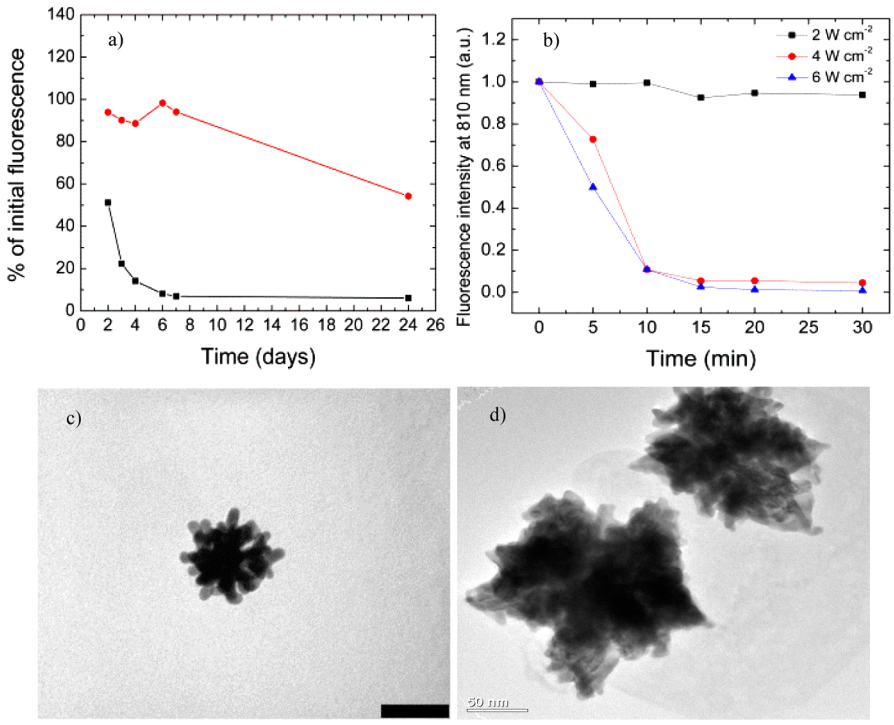


**Figure 5. (a) Temporal evolution of fluorescence intensity of (■) free ICG and (●) ICG complexed to BGNSH-HSA-ICG-FA nanoplatforms. Lines are to guide the eye. (b) Photostability of BGNSH-HSA-ICG-FA nanoplatforms after continuous illumination with NIR-light. (c) TEM image of one BGNSH-HSA-ICG-FA after 30 min of irradiation at 2 W cm$^{-2}$ and (d) after 5 min at 4 W cm$^{-2}$. Scale bar in (c) is 100 nm.**

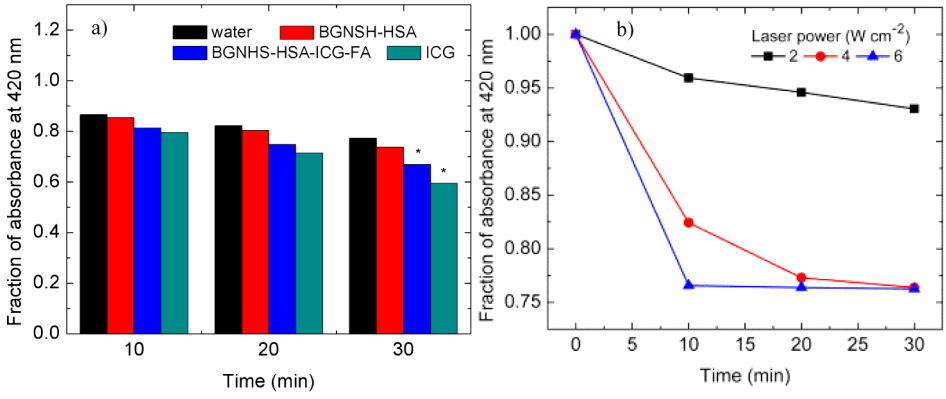


**Figure 6. (a) Absorbance decay of DPIBF after illumination of pure water, BGNSH-HSA, BGNSH-HSA-ICG-FA and ICG solutions with NIR light (808 nm) at 2 W cm$^{-2}$. (b) Decay of DPIBF absorbance at 420 nm discarding the contribution of photodegradation by laser and the contribution of thermodegradation induced by BGNSH-HSA at 2, 4, and 6 W cm$^{-2}$. Stars denoted statistically significant data ($P < 0.05$).**

the singlet oxygen production took place (Figure 6a). Also, $^1O_2$ production was enhanced as the irradiated energy input was larger. Interestingly, the $^1O_2$ production of BGNSH-HSA-ICG-FA nanoplatforms was slightly lower than that of free ICG at similar concentration provided that the effective laser energy for the production of singlet oxygen was lower in the former case than in the latter; that is, for BNSH-HSA-ICG-FA nanoplatforms laser energy is simultaneously absorbed by ICG and the metal shell to simultaneously produce singlet oxygen and heat, in agreement with previous works.[34,43,48] The $^1O_2$ generation rate of free ICG and BGNSH-HSA-ICG-FA nanoplatforms also decreased after first 10 min of irradiation, which is consistent with the change in fluorescence intensity of ICG and HSA-ICG-FA complex (Figure 6b).

To determine the potential use of this kind of nanoplatforms as potential fluorescence imaging contrast agents, *in vitro* and *in vivo* localization/biodistribution experiments were performed. Fluorescence NIR images provided by ICG fluorescence showed internalization of the nanoplatforms with an homogeneous distribution in the cytoplasm of HeLa cervical (Figure 7a–c) and MDA-MB-231 breast cancer cells (Supporting Information Figure S6) and, probably occurring *via* a receptor-mediated endocytosis pathway

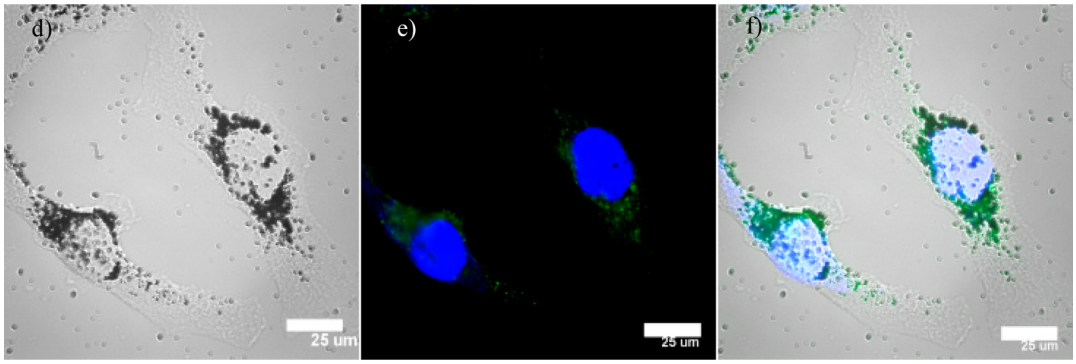


**Figure 7. (a) Transmission, (b) fluorescence, and (c) merged confocal NIR images of BGNSH-HSA-ICG-FA nanoplatform internalization inside HeLa cells. Nuclei were stained with DAPI (blue channel, $\lambda_{exc}$ = 355 nm), and ICG localization around nuclei was colored in green ($\lambda_{exc}$ = 712 nm).**

assuming that both kind of cells overexpressed folate receptors on their surface (see below).[66,67]

To analyze the potential use of the present nanoplatforms as imaging probes, a preliminary *in vivo* targeting visualization of the nanoplatforms was tested by implanting MDA-MB-231 cells subcutaneously into BALB/c nude mice. When the tumor reached approximately 100 $mm^3$ in size, intravenous administration of 10 mg/kg of BGNSH-HSA-ICG-FA into the mouse tail vein was performed. For comparison, FA-HSA/ICG-loaded PLGA NPs with the same dye concentration were also administered as a control. Monitorization of the nanoplatforms by measuring time-lapse *in vivo* NIR images with an IVIS Spectrum Imaging System revealed that the fluorescence intensity changed in the tumor region already after 2 h postinjection due to the localization of the nanoplatforms in the tumor by the combination of an enhanced permeation and retention effect (EPR effect) and a receptor-mediated endocytosis process if compared to BGNSH-HSA-ICG nanoplatforms (see differences in fluorescence signal intensities in Figure 8a and Supporting Information Figure S7). A gradual increase in fluorescence intensity observed in the tumor area with time indicated that the nanoplatforms progressively accumulated in such region, but a complete and absolute retention of the nanoplatforms seemed to be not completely achieved, as observed from some spreading of the fluorescence signal (Figure 8a). Hence, these observations suggest the need of an additional optimization of FA functionalization and/or the choice of an alternative ligand which would bind with larger affinity to other overexpressed receptors such as epidermal growth factor receptor, CD44, $\alpha_v\beta_3$ integrin, or transforming growth factor alpha (TGF-$\alpha$).[68,69] In addition, nanoplatforms were observed to be extensively retained at the tumor area for at least 48 h, as denoted by the larger fluorescence intensity if compared with that of FA-HSA/ICG-loaded PLGA NPs used also as additional control to qualitatively observe the potential role of the metal shell on biodistribution (Figure 8b). In the latter case, the progressive decrease

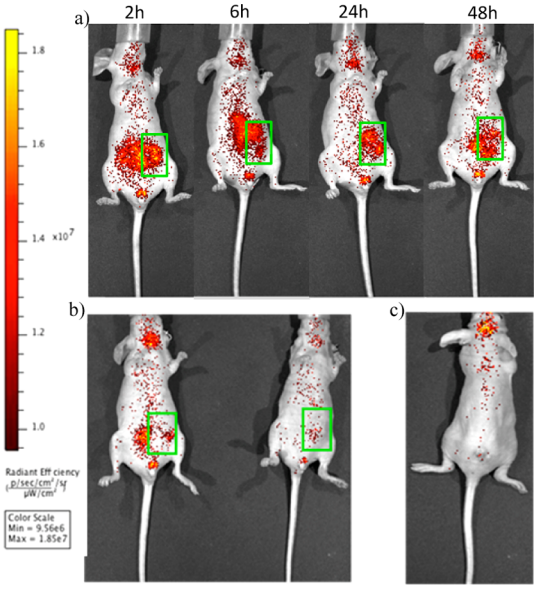


**Figure 8. (a) Biodistribution and localization of BGNSH-HSA-ICG-FA nanoplatforms at the tumor site (denoted by the green-squared region in the images) at different times after injection. (b) Biodistribution and localization of BGNSH-HSA-ICG-FA nanoplatforms (left) and FA-HSA/ICG-PLGA NPs (right) at the tumor site (green-squared region) after 96 h of injection. (c) Fluorescence image showing nanoplatform accumulation at the brain area. Fluorescence images were taken at $\lambda_{exc}$ = 710 nm and $\lambda_{em}$ = 840 nm.**

in fluorescence intensity in the tumor site originated from the clearance of the dye released from the PLGA NPs upon diffusion and matrix erosion.[70]

On the other hand, 3-D image reconstruction of the fluorescence images (Supporting Information Figure S8) also enabled us to determine that the nanoplatforms are eliminated through the reticuloendothelial system (RES), in particular, these are observed to be exclusively accumulated in the spleen, with almost no traces apparently in liver or lungs after 12 h postinjection. At longer circulation times, the nanoplatform accumulation was progressively reduced until completely disappeared. In addition, it is worth mentioning that a relatively intense fluorescence signal was

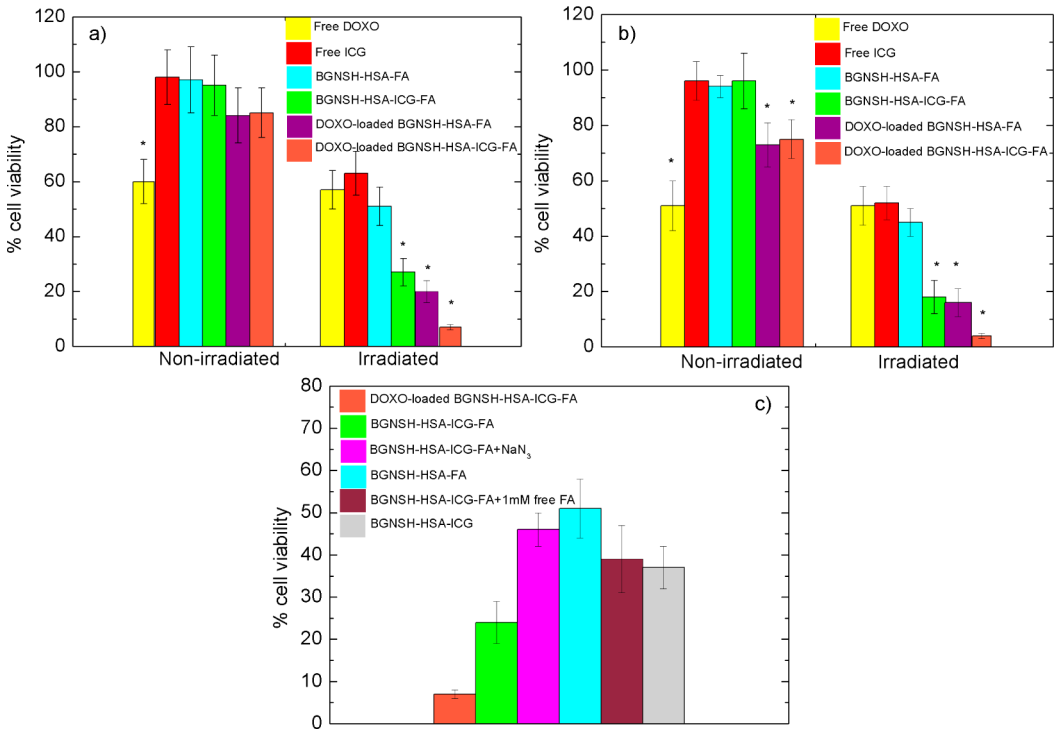


**Figure 9. Cell viability of (a) HeLa and (b) MDA-MB-231cells after 24 h of incubation in the absence and presence of NIR light irradiation (2 W cm$^{-2}$ at 808 nm in 3 intervals of 5 min each). Color code: yellow, free DOXO; red, free ICG; cyan, BGNSH-HSA-FA; green, BGNSH-HSA-ICG-FA; violet, DOXO-loaded BGNSH-HSA-FA; orange, DOXO-loaded BGNSH-HSA-ICG-FA nanoplatforms. (c) Cell viability of HeLa cells under irradiation in the presence of DOXO-loaded BGNSH-HSA-ICG-FA (orange), BGNSH-HSA-ICG-FA (green), BGNSH-HSA-ICG-FA + $NaN_3$ (magenta), BGNHS-HSA-FA (cyan), BGNHS-HSA-ICG-FA + 1 mM free FA (brown), and BGNSH-HSA-ICG (gray). Stars denoted statistically significant data ($P < 0.05$).**

unexpectedly observed around the brain area in the time scale of the experiments, which suggests the possible accumulation of the present nanoplatforms in such region (Figure 8). However, additional and more detailed tests are required to confirm this hypothesis and analyze the potential extent of nanoplatform accumulation, clearance mechanisms, and nanoplatform activity in order to explore later on potential uses of these nanomaterials as specific theranostic nanodevices for the treatment of brain pathologies.

Finally, we further evaluated *in vitro* the multidimensional therapeutic potential of the present BGNSH-HSA-ICG-FA nanoplatforms on systemic chemotherapy (DOXO), localized hyperthermia from the Au shell, and photodynamic activity provided by ICG molecules in the absence and presence of NIR laser irradiation through the cell-counting kit-8 cell proliferation assay (CCK-8). This test is based on the bioreduction of 2-(2-methoxy-4-nitrophenyl)-3-(4-nitrophenyl)-5-(2,4-disulfophenyl)-2*H*-tetrazolium monosodium salt (WST-8), which produces a water-soluble formazan dye in the presence of an electron carrier, 1-methoxy phenazine methosulfate (PMS).

Cell viabilities (CV) of HeLa and MDA-MB-231 cells treated with free DOXO, free ICG, BGNSH-HSA-FA, BGNSH-HSA-ICG-FA, DOXO-loaded BGNSH-HSA-FA, and DOXO-loaded BGNSH-HSA-ICG-FA in the absence and presence of NIR laser illumination after 24 h of incubation are shown in Figure 9a,b. The HSA-BGNSHs particles were completely nontoxic; DOXO-loaded BGNSH-HSA and DOXO-loaded BGNHS-HSAICG nanoplatforms also displayed low toxicities as a result of, on one hand, the slow diffusion of the drug through the metal shell which cannot inhibit tumor-cell proliferation (if compared with the largest cytoxicity of free DOXO) and, on the other, the low cytotoxicity of ICG, as observed from the reduced cytotoxicity values observed for the free dye. In comparison, NIR laser illumination (808 nm and 2 W cm$^{-2}$ for 3 intervals of 5 min each, see Methods section for details) of the nanoplatforms led to a noticeable increase. BGNHS-HSA-FA nanoplatforms decreased cell viability upon NIR irradiation as a consequence of the generation of the hyperthermic effect from the metal nanolayer, which led to protein denaturation and subsequent inhibition of normal cellular growth and proliferation[71] if compared to the nonirradiated samples. It should be stressed that BGNSH-HSA-ICG-FA nanoplatforms led to larger cell mortalities than either free ICG or BGNSH-HSA-FA after irradiation (Figure 9).

Given that the cytotoxicity of BGNSH-HSA-FA and free ICG was negligible in the absence of irradiation, this improved efficiency might be attributed to a possible enhanced cellular uptake of BGNSH-HSA-ICG-FA nanoplatforms and/or to a synergistic PDT/PTT effect.

To confirm that the synergistic PDT/PTT effect contributed to cell cytotoxicity, we incubated BGNSH-HSA-ICG-FA particles with HeLa cells in the presence of 100 mM sodium azide ($NaN_3$) for 30 min before irradiation provided that $NaN_3$ protects cells against PDT damage.[34] We observed that the phototoxicity of BGNSH-HSA-ICG-FA in the presence of $NaN_3$ turned to be quite similar to that of BGNSH-HSA-FA particles (Figure 9c). The targeting ligand, FA, also played an important role in improving the cell cytotoxic by favoring the internalization of the nanoplatforms. This can be directly observed when comparing the larger cell toxicity provided by BGNSH-HSA-ICG-FA nanoparticles regarding that of BGNSH-HSA-ICG ones. This fact is additionally corroborated when blocking folate receptors of HeLa cells with an excess of free FA molecules prior incubation of BGNSH-HSA-ICG-FA nanoplatforms, which led to similar cell toxicities as after incubation in the presence of BGNSH-HSA-ICG nanoparticles.

Notably, for example, BGNSH-HSA-ICG-FA nanoplatforms exhibited a synergistic cytotoxic effect in HeLa cells of 47.1% $((CV_{BGNSH\text{-}HSA\text{-}FA+laser} - CV_{BGNSH\text{-}HSA\text{-}ICG\text{-}FA+laser})/CV_{BGNSH\text{-}HSA\text{-}FA+laser})$ and 56.5% $(CV_{free\ ICG+laser} - CV_{BGNSH\text{-}HSA\text{-}ICG\text{-}FA+laser})/CV_{free\ ICG+laser})$ if compared with BGNSH-HSA-FA nanoplatforms and free ICG, respectively. On the other hand, the chemotherapeutic effect of DOXO also led to an enhanced cytotoxicity when loaded inside BGNSH-HSA-ICG-FA if compared to free DOXO and unloaded BGNSH-HSA-ICG-FA particles as a consequence of the remote and sustained controlled release of the chemotherapeutic drug, which is favored by the partial melting of the polymeric core, for additional cytotoxic activity against the target cancer cell line. In this regard, DOXO-loaded BGNSH-HSA-ICG-FA nanoplatforms exhibited an additional cytotoxic effect of 74.0% $((CV_{BGNSH\text{-}HSA\text{-}ICG\text{-}FA+laser} - CV_{DOXO\text{-}loaded\ BGNSH\text{-}HSA\text{-}ICG\text{-}FA+laser})/CV_{BGNSH\text{-}HSA\text{-}ICG\text{-}FA+laser})$ compared with unloaded BGNSH-HSA-ICG-FA nanoplatforms.

The mechanism by which the present multifunctional nanoplatforms cause toxicity to cells was elucidated by the Annexin V/Dead Cell assay. Cell death by apoptosis is accompanied by a change in cell membrane, manifested by the exposition of phosphatidyl serine (PS) on the surface while the membrane integrity remains intact. PS molecules in the surface of apoptotic cells can be detected by Annexin V, a protein with high affinity to PS. The proportion of live, dead, and apoptotic cells was quantified by flow cytometry (Supporting Information Figure S9). Experimental data (Table 1) confirmed that cell death caused by BGNSH-HSA, BGNSH-HSA-ICG, BGNSH-HSA-ICG-FA, and DOXO-BGNSH-HSA-ICG-FA under NIR irradiation (808 nm, 2 W $cm^{-2}$ for 15 min) was mainly through apoptosis, which is a more suitable cell death pathway for treatments in which a less inflammatory reaction is desired.[9]

**TABLE 1. Proportion of Live, Debris, and Apoptotic Cells after Incubation and Illumination with NIR Laser (808 nm, 2 W $cm^{-2}$ for 5 min)[a]**

| sample | live (%) | dead (%) | EA (%) | LA (%) | TA (%) |
|---|---|---|---|---|---|
| BGNSH-HSA | 57.62 | 3.79 | 19.04 | 19.55 | 38.59 |
| BGNSH-HSA-ICG | 33.83 | 5.23 | 19.09 | 41.85 | 60.94 |
| BGNSH-HSA-ICG-FA | 31.76 | 3.35 | 25.17 | 39.72 | 64.89 |
| DOXO-BGNSH-HSA-ICG-FA | 17.80 | 3.41 | 14.30 | 64.48 | 78.78 |

[a] EA, early apoptotic; LA, late apoptotic; TA, total apoptotic.

## CONCLUSIONS

In summary, we have successfully fabricated a potential smart theranostic nanoplatform composed of a chemotherapeutic agent (DOXO) and a polymer-based gold shell which additionally combines localized photothermal activity provided by the metal shell and generation of singlet oxygen species by an incorporated ICG photosensitizer under NIR light illumination. The gold nanolayer was functionalized with an HSA-ICG-FA complex to provide, on one hand, stealthiness to the nanoplatform and, on the other, photodynamic therapy, fluorescence-based imaging, and targetability abilities. In addition, the thickness of the protein layer was suitable to provide an enhancement of the dye fluorescence by the plasmonic coupling of the metal nanolayer. *In vitro* confocal fluorescence imaging confirmed the successful cell internalization of the hybrid nanoplatforms, while *in vivo* fluorescence imaging demonstrated that nanoplatforms are localized and retained in the tumor region for long time. The simultaneous combination of chemotherapy, hyperthermia, and oxygen reactive species led to enhanced *in vitro* cell cytotoxicity, as measured in two different cancer cell lines. Further studies are being developed to minimize light irradiation doses and nanoplatform concentrations by optimization of the synthetic protocols, to add new functionalities and to quantify the cytotoxic potential of the nanoplatforms *in vivo*.

## METHODS

**Materials.** Human serum albumin (HSA), indocyanine green (ICG), doxorubicin (DOXO), folic acid (FA), poly(D,L-lactide-*co*-glycolide) (PLGA) of 7−17 kDa with 50:50 lactide−glycolide ratio, Pluronic F127, hydrogen tetrachloroaureate(III) trihydrate ($HAuCl_3 \cdot 3H_2O$), *N*-(3-dimethylamniopropyl)-3-ethylcarbodiimide hydrochloride (EDC), sulfo-*N*-hydroxysuccinimide (Sulfo-NHS), 1,3-diphenylisobenzofuran (DPIBF), low molecular weight chitosan (LMW-chitosan, $M_W$ = 111 kDa), potassium carbonate anhydrous, sodium borohydride, sodium azide, sodium citrate tribasic, and ascorbic acid were purchased from Sigma−Aldrich (St. Louis, MO). ProLong Gold antifade reagent with DAPI was purchased from Invitrogen (Carlsbad, CA). DOXO HCl, fetal bovine serum (FBS), Dulbecco's modified Eagle's medium

(DMEM), fetal bovine serum (FBS), L-glutamine, penicillin/streptomycin, sodium pyruvate, and MEM nonessential amino acids (NEAA) were purchased from Fisher Scientific (Pittsburgh, PA). Dialysis membrane tubing (molecular weight cutoff ~3500) was purchased from Spectrum Laboratories, Inc. (Rancho Dominguez, CA). All other chemicals and solvents were of reagent grade (purchased from Sigma–Aldrich). Milli-Q water was used for all aqueous solutions. All glassware was washed with aqua regia and HF 5% (v/v) and extensively rinsed with water. All the chemicals were of analytical grade and used without further purification.

**Synthesis of BGNSHs.** PLGA-core gold-shell nanoconstructs (BGNSHs) were synthesized following a seeded-growth protocol based on previously protocols but with modifications.[72] First, PLGA NPs were synthesized by a nanoprecipitation process, using acetone as the organic solvent and F127 as a stabilizer agent. Briefly, in a typical preparation 25 mg of PLGA was dissolved in 2.5 mL of acetone. Subsequently, a suitable amount of DOXO (previously converted to its hydrophobic base form by addition of triethylamine, as reported in literature)[73] was added. This organic solution was added dropwise at 0.166 mL/min to 50 mL of F127 1% (w/v) in water at 10 °C with moderate stirring at 250 rpm. The mixed solution was homogenized with a sonicating tip at 100 W in an ice bath for 15 min. Acetone, nonencapsulated DOXO, and excess stabilizer were eliminated by stirring for 4 h and subsequent centrifugation twice at 9000 rpm for 30 min. DOXO concentration in the supernatant was measured by UV–vis spectroscopy by using a previously obtained-drug calibration curve. The final pellet was dispersed in 25 mL of water by vortexing for 30 s and filtered through 0.45 $\mu$m filters (Merck Millipore). PLGA NPs had a hydrodynamic diameter and $\zeta$-potential of 100 $\pm$ 20 nm and $-39 \pm 8$ mV, respectively.

To grow the gold nanolayer around the PLGA dielectric NP core, 5 mL of PLGA NPs (~$1.7 \times 10^{13}$ NPs mL$^{-1}$) was incubated for 4 h with 0.25 mL of chitosan. Chitosan, a biocompatible polycation, was adsorbed on the negative surface of PLGA NPs by electrostatic attraction, inverting the NPs surface charge to +4 mV. Excess of chitosan was eliminated by centrifugation twice at 9000 rpm for 15 min and 20 °C. Then, positively charged PLGA NPs were incubated for 4 h with 5 mL of citrate-capped Au seeds prepared following a methodology previously reported by Jana *et al.*[74] Nonattached gold seeds were eliminated by centrifugation twice at 7000 rpm for 15 min at 20 °C. Subsequently, an Au growth solution was prepared by dissolving 0.05 g of potassium carbonate in 98 mL of DI water and subsequent addition of 2 mL of 0.025 M $HAuCl_4 \cdot 3H_2O$; the solution was aged 24 h prior use. The growth of the Au shell was achieved by mixing 1 mL of PLGA NPs-seed precursor with 20 mL of the Au growth solution and subsequent reduction with 25 $\mu$L of 0.5 M ascorbic acid. PGNHs were immediately formed, as noticed by the blue coloration of the mixture solution. BGNSHs were left stand overnight and washed twice by centrifugation at 3500 rpm for 15 min and 20 °C

**HSA-ICG Complex.** Indocyanine green (ICG) was noncovalently conjugated to human serum albumin (HSA) by mixing both reactants under ambient conditions. Typically, 10 mL of 5 $\mu$M HSA, previously incubated in an excess of glutathione (50 mM) to destabilize intramolecular disulfide bridges and purified by dyalisis, and 10 mL of 30 $\mu$M ICG both in 50 mM MES buffer at pH 6 were mixed and shaken for 4 h at ambient temperature. Then, to remove unbound ICG, the mixture was dialyzed for 24 h against MES buffer with a cellulose dialysis membrane with MWCO of 3500 Da. Absorbance peaks of the protein-dye complex ($\lambda_{max}$ = 780 nm) and bare protein ($\lambda_{max}$ = 280 nm) were monitored to account for free-dye removal. The concentration of bound ICG was determined after subtraction of the ICG concentration in the supernatant to that initially added. The HSA-ICG solution complex was stored at 4 °C and protected from light before use within next 12 h.

**Folic Acid Activation and Conjugation to HSA-ICG Complexes.** Folic acid was reacted with EDC and sulfo-NHS to generate an active species, FA*, and covalently attached to the HSA-ICG complex. First, 1 mL of 5 mM folic acid in MES 50 mM (pH 6) was mixed with 3 mg of *N*-(3-dimethylaminopropyl)-*N*′-ethylcarbodiimide hydrochloride (EDC) and 3 mg of *N*-hydroxisulfosuccinimide (sulfo-NHS). This mixture was reacted for 20 min at ambient temperature and protected from light. FA* was reacted with HSA-ICG in order to form a covalent bond between the activated FA* and amine groups of HSA. A total of 50 $\mu$L of 5 mM FA* was mixed with 10 mL of 5 $\mu$M HSA-ICG in a 5:1 molar ratio. The product was dialyzed for 24 h against MES buffer with a cellulose membrane (MWCO 3500 Da) to eliminate unreacted FA* and remaining reaction byproducts. HSA-ICG complexes displayed two new peaks at *ca.* 280 and 360 nm, which correspond to FA (Supporting Information Figure S10) confirming the formation of HSA-ICG-FA complex. The number of FA molecules conjugated to HSA was calculated with an UV–vis calibration curve of FA (Supporting Information Figure S11). This curve was prepared by making dilutions of a stock solution of FA, and measuring their absorbance spectra. Absorbance at 280 and 360 nm was plotted against concentration and fitted to a linear curve. The concentration of FA in the complexes was found to be *ca.* 3 molecules of FA per HSA-ICG complex entity.

**Adsorption of HSA-ICG-FA on BGNSHs.** In a typical preparation, 2 mL of BGNSHs (~$1 \times 10^{11}$ NPs mL$^{-1}$) with an optical density (OD) set to 1 at 800 nm was mixed with 0.5 mL of the HSA-ICG-FA solution complex (2.4 $\mu$M HSA) previously obtained for 48 h under stirring in the dark. Afterward, BGNSH-HSA-ICG-FA nanoconjugates were centrifuged three times for 15 min at 3500 rpm and 20 °C in order to eliminate nonadsorbed complexes and resuspended in PBS (pH 7.4) buffer solution. The absorbance of the supernatant was closely monitored to account for unbound HSA-ICG-FA concentration in the supernatant in order to calculate the amount of ICG molecules on the nanoshells (set to *ca.* ~5.0 $\pm$ 0.4 $\mu$M). Finally, to further stabilize the protein coating, to 1 mL of BGNSH-HSA-ICG-FA nanoconjugates ($5 \times 10^{10}$ NPs mL$^{-1}$) in PBS (pH 7.4) was added *N*-(3-dimethylaminopropyl)-*N*-ethylcarbodiimide hydrochloride (5 mg, 25 mmol) and *N*-sulfo-hydroxysulfosuccinimide (5 mg, 25 mmol). The reaction was carried out for 2 h at room temperature. Crosslinked BGNSH-HSA-ICG-FA complexes were purified with desalting zeba spin columns (Fisher Scientific).

**Nanoplatform Characterization.** Nanoplatform sizes were obtained by dynamic light scattering (DLS) at 25 °C by means of an ALV-5000F (ALV-GmbH, Germany) instrument with vertically polarized incident light ($\lambda$ = 488 nm) supplied by a diode-pumped Nd:YAG solid-state laser (Coherent, Inc., CA) operated at 2 W, and combined with an ALV SP-86 digital correlator (sampling time 25 ns to 100 ms). NP sizes and morphologies were also acquired by transmission and scanning electron microscopy (TEM and SEM, respectively) by means of a Phillips CM-12 and a Carl Zeiss Libra 200 Fm Omega (for TEM), and FESEM ultra Plus electronic microscopes (for SEM) operating at 120 and 20 kV, respectively. Electron diffraction X-ray spectroscopy (EDX) was also performed using the same instrument as for SEM imaging. Samples were prepared for analysis by evaporating a drop of the hybrid NP dispersion on a carbon-coated copper grid without staining (TEM) or on a silicon wafer (SEM). $\zeta$-potentials were measured with a Zetasizer Nano ZS (Malvern, U.K.) using disposable folded capillary cells. Samples were measured in triplicate in PBS (pH 7.4) at 25 °C. The gold concentration in solution was determined by inductively coupling plasma–mass spectrometry (ICP-MS) in a Varian 820-MS equipment (Agilent Technologies). The corresponding concentration of BGNSH-HSA-ICG-FA particles was calculated by assuming a sphere model of *ca.* 100 nm diameter. UV–vis spectra were measured in a Cary Bio 100 UV–vis spectrophotometer (Agilent Technologies). Fluorescence spectra were monitored in a Cary Eclipse spectrophotometer (Agilent Technologies).

**NIR-Laser Induced Temperature Increase.** Temperature increment tests were performed with a continuous wave fiber-coupled diode laser source of 808 nm wavelength (50 W, Oclaro, Inc., San Jose, CA). The laser was powered by a Newport 5700-80 regulated laser diode driver (Newport Corporation, Irvine, CA). A 200-$\mu$m-core optical fiber was used to transfer laser power from the laser unit to the target solution, and equipped with a lens telescope mounting accessory at the output, which allowed for tuning of the laser spot size in the range 1–10 mm. The output power was independently calibrated using an optical power

meter (Newport 1916-C) and laser spot size was previously measured with a laser beam profiler (Newport LBP-1-USB), which was placed at the same distance (8 cm) between the lens telescope output and the quartz cuvette (or the 96-well plate). For measuring the temperature change mediated by the present BGNSH-HSA-ICG-FA, 2 mL of BGNSH-HSA-ICG-FA conjugates, PBS buffer containing 10% (v/v) FBS, BGNSHS and free ICG samples were placed in a quartz cuvette and irradiated for 10 min at 2 W $cm^{-2}$. The temperature of samples was measured with a type J thermocouple linked to a digital thermometer inserted into the solution.

**NIR-Laser Triggered Release of DOXO.** Release kinetics of DOXO from BGNSH-HSA-ICG-FA was assessed *in vitro* at 37 °C in PBS buffer (pH 7.4) containing 10% (v/v) fetal bovine serum. Briefly, 5 mL of DOXO-loaded BGNSH-HSA-ICG-FA with known DOXO concentration (3 $\mu$M) was placed in centrifuge tubes (in triplicate). Samples were maintained in a 37 °C bath with constant stirring. The samples were irradiated over a period of 10 min. Each hour, 500 $\mu$L of sample was taken and centrifuged at 3500 rpm for 10 min at 20 °C. The supernatant was carefully extracted and its fluorescence at 594 nm was measured in a Cary Eclipse spectrophotometer (Agilent Technologies, Spain) for quantification of released DOXO with a calibration curve. After centrifugation and supernatant extraction, the settled DOXO-loaded BGNSH-HSA-ICG-FA was resuspended in 500 $\mu$L with fresh buffer and returned to the original sample.

***In Vitro* Singlet Oxygen Generation.** The generation of singlet oxygen *in vitro* was performed by following the decay of the absorbance peak at 420 nm of 1,3-diphenylisobenzofurane (DPIBF), which is a specific singlet oxygen trap.[25] Briefly, 2 mL of sample (deionized water, free ICG, BGNSH-HSA, or BGNSH-HSA-ICG-FA conjugates) was placed in a quartz cuvette, and 100 $\mu$L of 1 mM DPIBF in ethanol was added. Concentration of free ICG and ICG bound to BGNSH-HSA-ICG-FA was *ca.* 5 $\mu$M. The UV−vis spectrum of samples before illumination was recorded and taken as the initial (100%) absorbance value. The sample was magnetically stirred and illuminated with NIR-light (808 nm) for 10 min; then, the UV−vis spectra was recorded and the process was repeated two more times. The total illumination time was 30 min. The singlet oxygen generation was qualitatively determined at three different laser powers densities: 2, 4, and 6 W $cm^{-2}$.

**Tumor Cells.** MDA-MB-231 adenocarcinoma breast and HeLa cervical cancer cells from Cell Biolabs (San Diego, CA) were used for *in vitro* studies. Cells were grown at standard culture conditions (5% $CO_2$ at 37 °C) in Dulbecco's modified Eagle's medium (DMEM) supplemented with 10% fetal bovine serum (FBS), 2 mM L-glutamine, 1% penicillin/streptomycin, 1 mM sodium pyruvate, and 0.1 mM MEM nonessential amino acids (NEAA).

**Cellular Uptake by Fluorescence Microscopy.** Cellular uptake of BGNSH-HSA-ICG-FA was followed by confocal fluorescence microscopy by seeding MDA-MB-231 and HeLa cells on poly-L-lysine coated glass coverslips (12 × 12 mm) placed inside 6-well plates (1.5 × $10^5$ cells/well with 3 mL of DMEM), and grown for 24 h at standard culture conditions. Then, the conjugates were added to cells (200 $\mu$L in PBS, pH 7.4, 1 × $10^{10}$ particles/mL). After 6 h of incubation, the NP-containing cells were washed three times with PBS, fixed with paraformaldehyde 4% (w/v) for 10 min, washed with PBS, pH 7.4, treated with Triton X-100 (permeabilizer) for 10 min, and finally washed again with PBS pH 7.4. Then, coverslips were mounted on glass slides, stained with DAPI (Invitrogen), and cured for 24 h at −20 °C. Samples were visualized at 63× using a wide field fluorescence microscope (Leica DMI6000B, Leica Microsystems, Germany) using blue channel for DAPI, $\lambda_{exc.}$ 350 nm, red channel for ICG ($\lambda_{exc.}$ 760 nm), and transmitted light in differential interference contrast (DIC) mode.

***In Vitro* Cell Cytotoxicity.** Cytotoxicity of nanoplatforms was tested *in vitro* by the CCK-8 cytotoxicity assay. Breast MDA-MB-231 and cervical HeLa cancer cells with an optical confluence of 80−90% were seeded into 96-well plates (100 $\mu$L, 1.5 × $10^4$ cells/well) and grown for 24 h at standard culture conditions in 100 $\mu$L growth medium. After 24 h of incubation at 37 °C and 5% $CO_2$, 50 $\mu$L of free DOXO (3 $\mu$M), free ICG (5 $\mu$M), BGNSH-HSA-FA, BGNSH-HSA-ICG (5 $\mu$M ICG), BGNSH-HSA-ICG-FA (5 $\mu$M ICG), DOXO-loaded BGNSH-HSA-FA (3 $\mu$M DOXO), and DOXO-loaded BGNSH-HSA-ICG-FA (3 $\mu$M DOXO, 5 $\mu$M ICG) was added to the wells. Some wells were left without particles as a negative control (blank) adding additional 50 $\mu$L of PBS. After 6 h of incubation, the culture medium was discarded, the cells were washed with 10 mM PBS, pH 7.4, several times, and new culture medium (100 $\mu$L) was added (previously aerated for 2 min) and incubated for 1 h. A set of cells was illuminated with 808 nm laser at 2 W $cm^{-2}$ for 5 min and then incubated 15 min. This process was repeated twice more. Then, cells were left incubated for additional 17 h. Another set of cells was left without illumination in order to determine the intrinsic cytotoxicity of the nanoplatforms. In some wells, 1 mM folic acid was added to block the specific receptors on the cell surface. After 24 h total incubation, 10 $\mu$L of CCK-8 reagent was added to each well, and after 2 h the absorption at 450 nm of cell, samples was measured with an UV−vis microplate absorbance reader (Bio-Rad model 689). Cell viability was calculated as follows:

$$\%CV = \frac{Abs_{sample}}{Abs_{blank}} \times 100$$

where $Abs_{sample}$ is absorbance at 450 nm for samples and $Abs_{blank}$ is absorbance for controls without nanoplatforms and in the absence of illumination.

**Annexin V/Dead Cell Apoptosis Assay.** HeLa cells were treated with BGNS-HSA, BGNSH-HSA-ICG, BGNSH-HSA-ICG-FA, DOXO-BGNSH-HSA-ICG-FA and with 2 $\mu$g $mL^{-1}$ DOXO as positive control for apoptosis. Untreated cells were used as negative (live) control. After 6 h of incubation with NPs or DOXO, the medium was changed by fresh medium and cells were illuminated with laser at 2 W $cm^{-2}$ for 5 min. After 24 h, cells were trypsinized and redispersed in 500 $\mu$L of fresh medium (7.5 × $10^4$ cells $mL^{-1}$). Then, 100 $\mu$L of cells was mixed with 100 $\mu$L of Annexin V/Dead Cell reagent and incubated for 20 min in the dark at ambient temperature. Finally, flow cytometry was assayed using a Millipore Muse cell analyzer (Millipore).

**Statistical Analysis.** All values shown are in mean ± SD unless otherwise stated. Analyses were done by unpaired Student's *t* test and considered significant at $P < 0.05$.

***In Vivo* Imaging and Biodistribution.** To assess the *in vivo* tracking of the nanoplatforms, 3 × $10^6$ cells from a MDA-MB-231 cell line were injected in the dorsal flank of immunodeficient BALB/c nude mice.[32] One week upon injection, cell implantation was checked by registering the fluorescent activity of the cells. We next injected 10 mg/kg of either HSA-ICG-FA/NGHSH nanoplatforms or ICG-loaded PLGA NPs (as a control) in the mice tail vein and registered the *in vivo* fluorescent activity ($\lambda_{exc}$ = 710 nm/$\lambda_{em}$ = 840 nm) with a IVIS Spectrum imaging system (Caliper Life Sciences, Perkin-Elmer) at different time intervals.

*Conflict of Interest:* The authors declare no competing financial interest.

*Acknowledgment.* Authors thank Ministerio de Economía y Competitividad (MINECO) for research project MAT 2010-17336 and SAF2009-08629 (J.A.C.), Xunta de Galicia for research grant CN2012/072, and Fundación Ramón Areces for additional financial support. S.B. also thanks MINECO for her Ramon y Cajal fellowship. Authors also specially thank staff of Instituto de Ortopedia y Banco de Tejidos Musculoesqueléticos of the Universidad de Santiago de Compostela, and specially to Maite Silva, for helpful assistance during *in vitro* cell experiments. A.T. and M.A.-M. thank Mexico's National Council of Science and Technology (CONACYT) for grants No. 203907 and No. 203732, respectively.

*Supporting Information Available:* Scheme of the synthesis of BGNSHs; EDX spectrum, SEM images and bit maps of BGNSHs; scheme of the conjugation of ICG and folic acid to HSA hydrodynamic radii of HSA-ICG-FA complexes at different stages of the conjugation; $\zeta$-potential of HSA complexes in MES 50 $\mu$M (pH 6); hydrodynamic radii and $\zeta$-potential of complexes in PBS 10 mM (pH 7.4); time stability of BGNSH-HSA-ICG-FA nanoplatforms; TEM images of BGNSH-HSA-ICG-FA nanoplatforms after different irradiation conditions; confocal NIR image of BGNSH-HSA-ICG-FA nanoplatforms after internalization inside

MDA-MB-231 breast cancer cells; *in vivo* biodistribution of BGNSH-HSA-ICG nanoplatforms at different times; 3D reconstructed fluorescence images of BGNSH-HSA-ICG-FA nanoplatform accumulation in RES system; annexin V/dead cell flow cytometry profiles of BGNSH-HSA, BGNSH-HSA-ICG, BGNSH-HSA-ICG-FA and DOXO-BGNSH-HSA-ICG-FA nanoplatforms; UV−vis spectra of HSA-ICG complexes before and after reaction/dyalisis with FA*; UV−vis spectra and calibration curve of FA. This material is available free of charge *via* the Internet at http://pubs.acs.org.

## REFERENCES AND NOTES


1. Lammers, T.; Aime, S.; Hennink, W. E.; Storm, G.; Kiessling, F. Theranostic Nanomedicine. *Acc. Chem. Res.* **2011**, *44*, 1029–1038.
2. Ryu, J. H.; Koo, H.; Sun, I.-C.; Yuk, S. H.; Choi, K.; Kim, K.; Kwon, I. C. Tumor-Targeting Multi-Functional Nanoparticles for Thernostics: New Paradigm for Cancer Therapy. *Adv. Drug Delivery Rev.* **2012**, *64*, 1447–1458.
3. Mura, S.; Couvreur, P. Nanotheranostics for Personalized Medicine. *Adv. Drug Delivery Rev.* **2012**, *64*, 1394–1416.
4. Yang, Z.; Lee, J. H.; Jeon, H. M.; Han, J. H.; Park, N.; He, Y.; Lee, H.; Hong, K. S.; Kang, C.; Kim, J. S. Folate-Based Near-Infrared Fluorescent Theranostic Gemcitabine Delivery. *J. Am. Chem. Soc.* **2013**, *135*, 11657–11662.
5. Zheng, M.; Yue, C.; Ma, Y.; Gong, P.; Zhao, P.; Zheng, C.; Sheng, Z.; Zhang, P.; Wang, Z.; Cai, L. Single-Step Assembly of DOC/ICG Loaded Lipid-Polymer Nanoparticles for Highly Effective Chemo-Photothermal Combination Therapy. *ACS Nano* **2013**, *7*, 2056–2067.
6. Menon, J. U.; Jadeja, P.; Tambe, P.; Vu, K.; Yuan, B.; Nguyen, K. T. Nanomaterials for Photo-Based Diagnostic and Therapeutic Applications. *Theranostics* **2013**, *3*, 152–166.
7. Pan, D. Theranostic Nanomedicine with Functional Nanoarchitecture. *Mol. Pharmaceutics* **2013**, *10*, 781–782.
8. Caldorera-Moore, M. E.; Liechty, W. B.; Peppas, N. A. Responsive Theranostic Systems: Integration of Diagnostic Imaging Agents and Responsive Controlled Release Drug Delivery Carriers. *Acc. Chem. Res.* **2011**, *44*, 1061–1070.
9. Doane, T. L.; Burda, C. The Role of Nanoparticles in Nanomedicine: Imaging, Drug Delivery and Therapy. *Chem. Soc. Rev.* **2012**, *41*, 2885–2911.
10. Ma, X.; Zhao, Y.; Liang, X.-J. Theranostic Nanoparticles Engineered for Clinic and Pharmaceutics. *Acc. Chem. Res.* **2011**, *44*, 1114–1122.
11. Lee, G. Y.; Qian, W. P.; Wang, L.; Wang, Y. A.; Staley, C. A.; Satpathy, M.; Nie, S.; Mao, H.; Yang, L. Theranostic Nanoparticles with Controlled Release of Gemcitabine for Targeted Therapy and MRI of Pancreatic Cancer. *ACS Nano* **2013**, *7*, 2078–2089.
12. Khaletskaya, K.; Reboul, J.; Meilikhov, M.; Nakahama, M.; Diring, S.; Tsujimoto, M.; Isoda, S.; Kim, F.; Kamei, K.-I.; Fischer, R. A.; *et al.* Integration of Porous Coordination Polymers and Gold Nanorods into Core-Shell Mesoscopic Composites Toward Light-Induced Molecular Release. *J. Am. Chem. Soc.* **2013**, *135*, 10998–11005.
13. Hilderbrand, S. A.; Weissleder, R. Near-Infrared Fluorescence: Application to *in Vivo* Molecular Imaging. *Curr. Opin. Chem. Biol.* **2010**, *14*, 71–79.
14. Zhou, J.; Liu, Z.; Li, F. Upconversion Nanophosphors for Small-Animal Imaging. *Chem. Soc. Rev.* **2012**, *41*, 1323–1349.
15. Lovell, J. F.; Liu, T. W. B.; Chen, J.; Zheng, G. Activable Photosensitizers for Imaging and Therapy. *Chem. Rev.* **2010**, *110*, 2839–2857.
16. Celli, J. P.; Spring, B. Q.; Rizvi, I.; Evans, C. L.; Samkoe, K. S.; Verma, S.; Pogue, B. W.; Hasan, T. Imaging and Photodynamic Therapy: Mechanisms, Monitoring, and Optimization. *Chem. Rev.* **2010**, *110*, 2795–2838.
17. Choi, K. Y.; Liu, G.; Lee, S.; Chen, X. Theranostic Nanoplatforms for Simultaneous Cancer Imaging and Therapy: Current Approaches and Future Perspectives. *Nanoscale* **2012**, *4*, 330–342.
18. Huang, P.; Xu, Cheng; Lin, J.; Wang, C.; Wang, X.; Zhang, C.; Zhou, X.; Guo, S.; Cui, D. Folic Acid-Conjugated Graphene Oxide Loaded with Photosensitizers for Targeting Photodynamic Therapy. *Theranostics* **2011**, *1*, 240–250.
19. Huang, P.; Lin, J.; Wang, X.; Wang, Z.; Zhang, C.; He, M.; Wang, K.; Chen, F.; Li, Z.; Shen, G.; *et al.* Light-Triggered Theranostic Based on Photosensitizer-Conjugated Carbon Dots for Simultaneous Enhanced Fluorescence Imaging and Photodynamic Therapy. *Adv. Mater.* **2012**, *24*, 5104–5110.
20. Lin, J.; Wang, S.; Huang, P.; Wang, Z.; Chen, S.; Niu, G.; Li, W.; He, J.; Cui, D.; Lu, G.; *et al.* Photosensitizer-Loaded Gold Vesicles with Strong Plasmonic Coupling Effect for Imaging-Guided Photothermal/Photodynamic Therapy. *ACS Nano* **2013**, *7*, 5320–5329.
21. Bonnett, R. Photosensitizers of the Porphyrin and Phthalocyanine Series for Photodynamic Therapy. *Chem. Soc. Rev.* **1995**, *24*, 19–33.
22. Yun, S.; Zhi-long, C.; Xiao-xia, Y.; Peng, H.; Xin-ping, Z.; Xiao-xia, D. Magnetic Chitosan Nanoparticles as a Drug Delivery System for Targeting Photodynamic Therapy. *Nanotechnology* **2009**, *20*, 135102.
23. Huang, P.; Li, Z.; Lin, J.; Yang, D.; Gao, G.; Xu, C.; Bao, L.; Zhang, C.; Wang, K.; Song, H.; *et al.* Photosensitizer-Conjugated Magnetic Nanoparticles for *in Vivo* Simultaneous Magnetofluorescent Imaging and Targeting Therapy. *Biomaterials* **2011**, *32*, 3447–3458.
24. Huang, P.; Lin, J.; Yang, D.; Zhang, C.; Li, Z.; Cui, D. Photosensitizer-Loaded Dendrimer-Modified Multi-Walled Carbon Nanotubes for Photodynamic Therapy. *J. Controlled Release* **2011**, *152*, e33–e34.
25. Jin, C. S.; Lovell, J. F.; Chen, J.; Zheng, G. Ablation of Hypoxic Tumors with Dose-Equivalent Photothermal, but Not Photodynamic, Therapy Using a Nanostructured Porphyrin Assembly. *ACS Nano* **2013**, *7*, 2541–2550.
26. Hongying, Y.; Fuyuan, W.; Zhiyi, Z. Photobleaching of Chlorins in Homogeneous and Heterogeneous Media. *Dyes Pigm.* **1999**, *43*, 109–117.
27. Sitnik, T. M.; Hampton, J. A.; Henderson, B. W. Reduction of Tumour Oxygenation During and After Photodynamic Therapy *in Vivo*: Effects of Fluence Rate. *Br. J. Cancer* **1998**, *77*, 1386–1394.
28. Coutier, S.; Mitra, S.; Bezdetnaya, L. N.; Parache, R. M.; Georgakoudi, I.; Foster, T. H.; Guillemin, F. Effects of Fluence Rate on Cell Survival and Photobleaching in *Meta*-Tetra-(Hydroxyphenyl)Chlorin-Photosensitized Colo 26 Multicell Tumor Spheroids. *Photochem. Photobiol.* **2001**, *73*, 297–303.
29. Agostinis, P.; Berg, K.; Cengel, K. A.; Foster, T. H.; Girotti, A. W.; Gollnick, S. O.; Hahn, S. M.; Hamblin, M. R.; Juzeniene, A.; Kessel, D.; *et al.* Photodynamic Therapy of Cancer: An Update. *CA—Cancer J. Clin.* **2011**, *61*, 250–281.
30. Alkilany, A. M.; Thompson, L. B.; Boulos, S. P.; Sisco, P. N.; Murphy, C. J. Gold Nanorods: Their Potential for Photothermal Therapeutics and Drug Delivery Tempered by the Complexity of Their Biological Interactions. *Adv. Drug Delivery Rev.* **2012**, *64*, 190–199.
31. Zhang, Z.; Wang, J.; Chen, C. Gold Nanorods-Based Platforms for Light-Mediated Theranostics. *Theranostics* **2013**, *3*, 223–238.
32. Bagley, A. F.; Hill, S.; Rogers, G. S.; Bhatia, S. N. Plasmonic Photothermal Heating of Intraperoneal Tumors Though the Use of an Implanted Near-Infrared Source. *ACS Nano* **2013**, *7*, 8089–8097.
33. Yuan, H.; Fales, A. M.; Vo-Dinh, T. TAR Peptide-Functionalized Gold Nanostars: Enhanced Intracellular Delivery and Efficient NIR Photothermal Therapy Using Ultralow Irradiance. *J. Am. Chem. Soc.* **2012**, *134*, 11358–11361.
34. Wang, S.; Huang, P.; Nie, L.; Xing, R.; Liu, D.; Wang, Z.; Lin, J.; Chen, S.; Niu, G.; Lu, G.; *et al.* Single Continuous Wave Laser Induced Photodynamic/Plasmonic Photothermal Therapy Using Photosensitizer-Funcionalized Gold Nanostars. *Adv. Mater.* **2013**, *25*, 3055–3061.
35. Gobin, A. M.; Lee, M. H.; Halas, N. J.; James, W. D.; Drezek, R. A.; West, J. L. Near-Infrared Resonant Nanoshells for

Combined Optical Imaging and Photothermal Cancer Therapy. *Nano Lett.* **2007**, *7*, 1929–1934.
36. Loo, C.; Lowery, A.; Halas, N.; West, J.; Drezek, R. Immunotargeted Nanoshells for Integrated Cancer Imaging and Therapy. *Nano Lett.* **2005**, *5*, 709–711.
37. Bardhan, R.; Chen, W.; Perez-Torres, C.; Bartels, M.; Huschka, R. M.; Zhao, L. L.; Morosan, E.; Pautler, R. G.; Joshi, A.; Halas, N. J. Nanoshells with Targeted Simultaneous Enhancement of Magnetic and Optical Imaging and Photothermal Therapeutic Response. *Adv. Funct. Mater.* **2009**, *19*, 3901–3909.
38. Hong, C.; Kang, J.; Kim, H.; Lee, C. Photothermal Properties of Inorganic Nanomaterials as Therapeutic Agents for Cancer Thermotherapy. *J. Nanosci. Nanotechnol.* **2012**, *12*, 4352–4355.
39. Murakami, T.; Nakatsuji, H.; Inada, M.; Matoba, Y.; Umeyama, T.; Tsujimoto, M.; Isoda, S.; Hashida, M.; Imahori, H. Photodynamic and Photothermal Effects of Semiconduting and Metallic Single-Walled Carbon Nanotubes. *J. Am. Chem. Soc.* **2012**, *134*, 17862–17865.
40. Wang, L.; Shi, J.; Zhang, H.; Li, H.; Gao, Y.; Wang, Z.; Wang, H.; Li, L.; Zhang, C.; Chen, C.; *et al.* Synergistic Anticancer Effect of RNAi and Photothermal Therapy Mediated by Functionalized Single-Walled Carbon Nanotubes. *Biomaterials* **2013**, *34*, 262–274.
41. Singh, R.; Torti, S. V. Carbon Nanotubes in Hyperthermia Therapy. *Adv. Drug Delivery Rev.* **2013**, *65*, 2045–2060.
42. Markovic, Z. M.; Harhaji-Trajkovic, L. M.; Todorovic-Markovic, B. M.; Kepić, D. P.; Arsikin, K. M.; Jovanović, S. P.; Pantovic, A. C.; Dramićanin, M. D.; Trajkovic, V. S. *In Vitro* Comparison of the Photothermal Anticancer Activity of Graphene Nanoparticles and Carbon Nanotubes. *Biomaterials* **2011**, *32*, 1121–1129.
43. Tian, B.; Wang, C.; Zhang, S.; Feng, L.; Liu, Z. Photothermally Enhanced Photodynamic Therapy Delivery by Nano-Graphene Oxide. *ACS Nano* **2011**, *5*, 7000–7009.
44. Yang, K.; Hu, L.; Ma, X.; Ye, S.; Cheng, L.; Shi, X.; Li, C.; Li, Y.; Liu, Z. Multimodal Imaging Guided Photothermal Therapy Using Functionalized Graphene Nanosheets Anchored with Magnetic Nanoparticles. *Adv. Mater.* **2012**, *24*, 1868–1872.
45. He, J.; Huang, X.; Li, Y.-C.; Liu, Y.; Babu, T.; Aronova, M. A.; Wang, S.; Lu, Z.; Chen, X.; Nie, Z. Self-Assembly of Amphiphilic Plasmonic Micelle-Like Nanoparticles in Selective Solvents. *J. Am. Chem. Soc.* **2013**, *135*, 7974–7984.
46. Huang, X.; El-Sayed, I. H.; Qian, W.; El-Sayed, M. A. Cancer Cell Imaging and Photothermal Therapy in the Near-Infrared Region by Using Gold Nanorods. *J. Am. Chem. Soc.* **2006**, *128*, 2115–2120.
47. Kuo, W.-S.; Chang, C.-N.; Chang, Y.-T.; Yang, M.-H.; Chien, Y.-H.; Chen, S.-J.; Yeh, C.-S. Gold Nanorods in Photodynamic Therapy, as Hyperthermia Agents, and in Near-Infrared Optical Imaging. *Angew. Chem., Int. Ed.* **2010**, *49*, 2711–2715.
48. Jang, B.; Park, J.-Y.; Tung, C.-H.; Kim, I.-H.; Choi, Y. Gold Nanorod-Photosensitizer Complex for Near-Infrared Fluorescence Imaging and Photodynamic/Photothermal Therapy *in Vivo*. *ACS Nano* **2011**, *5*, 1086–1094.
49. Mi, Y.; Liu, X.; Zhao, J.; Ding, J.; Feng, S.-S. Multimodality Treatment of Cancer with Herceptin Conjugated, Thermomagnetic Iron Oxides and Docetaxel Loaded Nanoparticles of Biodegradable Polymers. *Biomaterials* **2012**, *33*, 7519–7529.
50. Lee, S.-M.; Park, H.; Choi, J.-W.; Park, Y. N.; Yun, C.-O.; Yoo, K.-H. Multifunctional Nanoparticles for Targeted Chemo-photothermal Treatment of Cancer Cells. *Angew. Chem., Int. Ed.* **2011**, *50*, 7581–7586.
51. Watanabe, Y.; Kumon, K. Assessment by Pulse Dye-Densitometry Indocyanine Green (ICG) Clearance Test of Hepatic Function of Patients before Cardiac Surgery: Its Value as a Predictor of Serious Postoperative Liver Dysfunction. *J. Cardiothorac. Vasc. Anesth.* **1999**, *13*, 299–303.
52. Desmettre, T.; Devoisselle, J. M.; Mordon, S. Fluorescence Properties and Metabolic Features of Indocyanine Green (ICG) as Related to Angiography. *Surv. Ophthalmol.* **2000**, *45*, 15–27.
53. Bardhan, R.; Grady, N. K.; Halas, N. J. Nanoscale Control of Near-Infrared Fluorescence Enhancement Using Au Nanoshells. *Small* **2008**, *4*, 1716–1722.
54. Sanchez-Gaytan, B. L.; Swanglap, P.; Lamkin, T. J.; Hickey, R. J.; Fakhraai, Z.; Link, S.; Park, S.-J. Spiky Gold Nanoshells: Synthesis and Enhanced Scattering Properties. *J. Phys. Chem. C* **2012**, *116*, 10318–10324.
55. Choi, J.-s.; Park, J. C.; Nah, H.; Woo, S.; Oh, J.; Kim, K. M.; Cheon, G. J.; Chang, Y.; Yoo, J.; Cheon, J. A Hybrid Nanoparticle Probe for Dual-Modality Positron Emission Tomography and Magnetic Resonance Imaging. *Angew. Chem., Int. Ed.* **2008**, *47*, 6259–6262.
56. Al-Saadi, A.; Yu, C. H.; Khutoryanskiy, V. V.; Shih, S.-J.; Crossley, A.; Tsang, S. C. Layer-by-Layer Electrostatic Entrapment of Protein Molecules on Superparmagnetic Nanoparticle: A New Strategy to Enhance Adsorption Capacity and Maintain Biological Activity. *J. Phys. Chem. C* **2009**, *113*, 15260–15265.
57. Strozyk, M. S.; Chanana, M.; Pastoriza-Santos, I.; Pérez-Juste, J.; Liz-Marzán, L. M. Protein/Polymer-Based Dual-Responsive Gold Nanoparticles with pH-Dependent Thermal Sensitivity. *Adv. Funct. Mater.* **2012**, *22*, 1436–1444.
58. Sperling, R. A.; Parak, W. J. Surface Modification, Functionalization and Bioconjugation of Colloidal Inorganic Nanoparticles. *Philos. Trans. R. Soc., A* **2010**, *368*, 1333–1383.
59. Chanana, M.; Rivera-Gil, P.; Correa-Duarte, M. A.; Liz-Marzán, L. M.; Parak, W. J. Physicochemical Properties of Protein-Coated Nanoparticles in Biologival Fluids and Cells before and after Proteolytic Digestion. *Angew. Chem., Int. Ed.* **2013**, *52*, 4179–4183.
60. Link, S.; El-Sayed, M. A. Size and Temperature Dependence of the Plasmon Absorption of Colloidal Gold Nanoparticles. *J. Phys. Chem. B* **1999**, *103*, 4212–4217.
61. Prodan, E.; Lee, A.; Nordlander, P. The Effect of a Dielectric Core and Embedding Medium on the Polarizability of Metallic Nanoshells. *Chem. Phys. Lett.* **2002**, *360*, 325–332.
62. Goy-López, S.; Juárez, J.; Alatorre-Meda, M.; Casals, E.; Puntes, V. F.; Taboada, P.; Mosquera, V. Physicochemical Characteristics of Protein-NP Bioconjugates: The Role of Particle Curvature and Solution Conditions on Human Serum Albumin Conformation and Fibrillogenesis Inhibition. *Langmuir* **2012**, *28*, 9113–9126.
63. Li, J.; Han, J.; Xu, T.; Guo, C.; Bu, X.; Zhang, H.; Wang, L.; Sun, H.; Yang, B. Coating Urchinlike Gold Nanoparticles with Polypyrrole Thin Shells to Produce Photothermal Agents with High Stability and Photothermal Transduction Efficiency. *Langmuir* **2013**, *29*, 7102–7110.
64. Valdes-Aguilera, O.; Cincotta, L.; Foley, J.; Kochevar, I. E. Photobleaching of a Cyanine Dye in Solution and in Membranes. *Photochem. Photobiol.* **1987**, *45*, 337–344.
65. Weishaupt, K. R.; Gomer, C. J.; Dougherty, T. J. Identification of Singlet Oxygen as the Cytotoxic Agent in Photo-Activation of a Murine Tumor. *Cancer Res.* **1976**, *36*, 2326–2329.
66. Meier, R.; Henning, T. D.; Boddington, S.; Tavri, S.; Arora, S.; Piontek, G.; Rudelius, M.; Corot, C.; Daldrup-Link, H. E. Breast Cancer: MR Imaging of Folate-Receptor Expression with the Folate-Specific Nanoparticle P1133. *Radiology* **2010**, *255*, 527–535.
67. García-Díaz, M.; Kawakubo, M.; Mroz, P.; Sagristà, M. L.; Mora, M.; Nonell, S.; Hamblin, M. R. Cellular and Vascular Effects of the Photodynamic Agent Temocene Are Modulated by the Delivery Vehicle. *J. Controlled Release* **2012**, *162*, 355–363.
68. Dickson, R. B.; Bates, S. E.; McManaway, M. E.; Lippman, M. E. Characterization of Estrogen Responsive Transforming Activity in Human Breast Cancer Cell Lines. *Cancer Res.* **1986**, *46*, 1707–1713.
69. Mi, Z.; Guo, H.; Russell, M. B.; Liu, Y.; Sullenger, B. A.; Kuo, P. C. RNA Aptamer Blockade of Osteoponin Inhibits Growth and Metastasis of MDA-MB231 Breast Cancer Cells. *Mol. Ther* **2008**, *17*, 153–161.
70. Zolnik, B. S.; Leary, P. E.; Burgess, D. J. Elevated Temperature Accelerated Release Testing of PLGA Microspheres. *J. Controlled Release* **2006**, *112*, 293–300.

71. Hanahan, D.; Weinberg, R. A. The Hallmarks of Cancer. *Cell* **2000**, *100*, 57–70.
72. Yang, J.; Lee, J.; Kang, J.; Oh, S. J.; Ko, H.-J.; Son, J.-H.; Lee, K.; Suh, J.-S.; Huh, Y.-M.; Haam, S. Smart Drug-Loaded Polymer Gold Nanoshells for Systemic and Localized Therapy of Human Epithelial Cancer. *Adv. Mater.* **2009**, *21*, 4339–4342.
73. Jain, T. K.; Richey, J.; Strand, M.; Leslie-Pelecky, D. L.; Flask, C. A.; Labhasetwar, V. Magnetic Nanoparticles with Dual Functional Properties: Drug Delivery and Magnetic Resonance Imaging. *Biomaterials* **2008**, *29*, 4012–4021.
74. Jana, N. R.; Gearheart, L.; Murphy, C. J. Wet Chemical Synthesis of High Aspect Ratio Cylindrical Gold Nanorods. *J. Phys. Chem. B* **2001**, *105*, 4065–4067.
75. Iglesias, P.; Fraga, M.; Costoya, J. A. Definign Hypoxic Microenvironments by Non-Invasive Functional Optical Imaging. *Eur. J. Cancer* **2013**, *49*, 264–271.